

## OPEN ACCESS

EDITED BY  
Qiyu Jin,  
Inner Mongolia University, China

REVIEWED BY  
Huibin Chang,  
Tianjin Normal University, China  
Zhifeng Pang,  
Henan University, China

\*CORRESPONDENCE  
Weijing Liu  
✉ xiaodou7356@126.com  
Yuanquan Wang  
✉ wangyuanquan@scse.hebut.edu.cn

RECEIVED 02 August 2023  
ACCEPTED 06 September 2023  
PUBLISHED 04 October 2023

CITATION  
Wang D, Dang X, Liu W and Wang Y (2023)  
Image segmentation using active contours with  
image structure adaptive gradient vector flow  
external force.  
*Front. Appl. Math. Stat.* 9:1271296.  
doi: 10.3389/fams.2023.1271296

COPYRIGHT  
© 2023 Wang, Dang, Liu and Wang. This is an  
open-access article distributed under the terms  
of the [Creative Commons Attribution License  
\(CC BY\)](https://creativecommons.org/licenses/by/4.0/). The use, distribution or reproduction  
in other forums is permitted, provided the  
original author(s) and the copyright owner(s)  
are credited and that the original publication in  
this journal is cited, in accordance with  
accepted academic practice. No use,  
distribution or reproduction is permitted which  
does not comply with these terms.

# Image segmentation using active contours with image structure adaptive gradient vector flow external force

Dong Wang<sup>1</sup>, Xing Dang<sup>1</sup>, Weijing Liu<sup>1\*</sup> and Yuanquan Wang<sup>2\*</sup>

<sup>1</sup>Tianjin Key Lab of Aerospace Intelligent Equipment Technology, Tianjin Institute of Aerospace Mechanical and Electrical Equipment, Tianjin, China, <sup>2</sup>School of Artificial Intelligence, Hebei University of Technology, Tianjin, China

**Introduction:** Gradient vector flow (GVF) has been proven as an effective external force for active contours. However, its smoothness constraint does not take the image structure into account, such that the GVF diffusion is isotropic and cannot preserve weak edges well.

**Methods:** In this article, an image structure adaptive gradient vector flow (ISAGVF) external force is proposed for active contours. In the proposed ISAGVF model, the smoothness constraint is first reformulated in matrix form, and then the image structure tensor is incorporated. As the structure tensor characterizes the image structure well, the proposed ISAGVF model can be adaptive to image structure, and the ISAGVF snake performs well on weak edge preservation and deep concavity convergence while possessing some other desirable properties of the GVF snake, such as enlarged capture range and insensitivity to initialization.

**Results:** Experiments on synthetic and real images manifest these properties of the ISAGVF snake.

## KEYWORDS

image segmentation, active contour, gradient vector flow, image structure tensor, diffusion tensor

## 1. Introduction

Snakes or active contours are dynamic curves defined within an image domain that can move under the influence of internal and external forces [1]. Usually, the internal force comes from the geometrical properties of the contours and the external force is computed from the image data so that the snake will conform to an object boundary or other desired features within an image. The active contour model has been one of the most successful methods for region of interest (ROI) segmentation, and it can be grouped into two categories: parametric active contours [1] and geometric active contours [2–12]. Although deep learning-based methods launch an upsurge of image segmentation at present [13–17], the active contours are still an active topic (e.g., [18–29]), and we also focus on parametric active contours in this study.

As the external force plays a leading role in the evolution of active contours, and that of the traditional snake model is derived as the gradient vector of the edge map, the traditional snakes suffer from initialization sensitivity and concavity convergence. To this end, several useful external forces have been proposed, such as the balloon forces [30, 31]. However, both issues were not solved satisfactorily until the emergence of the gradient vector flow (GVF) [32]. The GVF snake has an enlarged capture range and can move into the concave boundary. Since the effectiveness of the GVF model became apparent, it became the focus of many studies and there have been many improved variants, e.g., the GGVF [33], CN-GGVF [34], harmonic gradient vector flow (HGVF) [35], GVF based on the minimal surface [36] and

adaptive diffusion flow (ADF) based on the harmonic surface [37], motion gradient vector flow (MGVF) [38], ILGVF [39], NBGVF [40], gradient vector convolution (GVC) [41], VEF [42], BVF [43], normal gradient vector flow (NGVF) [44], dynamic directional gradient vector flow (DDGVF) [45], EPGVF [46], GVFOM [47], and GVF based on augmented Lagrangian [48]. Additionally, there are some other interesting applications of the gradient vector flow (e.g., [49–52]). Very recently, Makhanov, etc., proposed some interesting studies on the initialization of the GVF snake [53–56] and Jaouen et al. [57] proposed a vector field for image enhancement, which resembles the GVF field.

Although the GVF model has been proven to be effective and widely employed in image segmentation, the smoothness constraint in GVF does not take into account the image structure and suffers from weak edge leakage and a failure to converge to long and thin indentations. In this study, a novel model called image structure adaptive gradient vector flow (ISAGVF) is proposed. In the ISAGVF model, the smoothness constraint in the GVF model is first reformulated into matrix form, and then the image structure tensor is incorporated into the matrix form energy so that the final diffusion equations for the ISAGVF exhibit an anisotropic diffusion behavior. As a result, the ISAGVF snake can preserve weak edges very well and converge to long and thin indentations. The basic idea of the ISAGVF model has been reported as an abstract in [58].

The remainder of this paper is organized as follows. In the Section 2, the GVF snake is briefly reviewed, and then the proposed ISAGVF algorithm is described in detail in the Section 3. In Section 4, a large number of examples and comparison results are reported to confirm the effectiveness of our model, and the conclusion is drawn in the final section.

## 2. Background: the snake model and gradient vector flow

Kass et al. defined the active contour model [1] as an elastic curve  $c(s) = [x(s), y(s)]$ ,  $s \in [0, 1]$ , that moves through the spatial domain of an image by minimizing the following energy functional:

$$E_{Snake} = \int_0^1 \left[ \frac{1}{2}(\alpha |c'(s)|^2 + \beta |c''(s)|^2) + \nabla E_{ext}(c) \right] ds, \quad (1)$$

where  $c'(s)$  and  $c''(s)$  denote the first and second derivative of  $c(s)$  with respect to the arc  $s$ , respectively,  $\alpha$  and  $\beta$  are weighting parameters that control the continuity and smoothness of the contour, respectively. The external energy  $E_{ext}$  comes from the image data, such as boundaries. The typical external force for an image  $I$  is  $\nabla E_{ext} = -\nabla |\nabla I|^2$ . A snake that minimizes  $E_{snake}$  must satisfy the following Euler-Lagrange equation:

$$\alpha c''(s) - \beta c''''(s) - \nabla E_{ext} = 0. \quad (2)$$

Xu and Prince suggested taking the above equation as a force balance equation of internal force and external force, as follows,

$$F_{int} + F_{ext} = 0, \quad (3)$$

where  $F_{int} = \alpha c''(s) - \beta c''''(s)$  and  $F_{ext} = -\nabla E_{ext}$ . As  $F_{ext}$  comes from the gradient of the edge map  $|\nabla I|^2$ , it is non-zero

only near edges; as a result, the traditional snake is sensitive to initialization and a failure to converge to concavity. To overcome these shortcomings, Xu and Prince suggest replacing  $F_{ext}$  with a more general one by proposing the gradient vector flow (GVF) [32], which is obtained by minimizing the following energy:

$$E_{GVF} = \iint \mu(u_x^2 + u_y^2 + v_x^2 + v_y^2) + |\nabla f|^2 |v - \nabla f|^2 dx dy, \quad (4)$$

where  $\mathbf{v}(x, y) = [u(x, y), v(x, y)]$  is the GVF vector,  $f$  is the edge map of an image, i.e.,  $f = \nabla G_\sigma * I$ , and  $\mu$  is a regularization parameter. It can be observed that when  $f$  is large at edge points, the second term dominates the energy in (4) and the GVF vector  $\mathbf{v}(x, y)$  approximately equals  $\nabla f$ , while  $f$  is small or even zero far away from edges; the first term in (4) is dominant and the GVF vector  $\mathbf{v}(x, y)$  varies smoothly, and as a result, the GVF snake has a large capture range and can converge to concavity. To minimize the  $E_{GVF}$ , it is converted to solve the following Euler-Lagrange equations:

$$\begin{cases} \frac{\partial u}{\partial t} = \mu \nabla^2 u - |\nabla f|^2 (u - f_x) \\ \frac{\partial v}{\partial t} = \mu \nabla^2 v - |\nabla f|^2 (v - f_y) \end{cases}, \quad (5)$$

where  $\nabla^2$  is the Laplacian operator. The generalized GVF (GGVF) model is obtained by replacing the constant parameter  $\mu$  with a spatially varying weighting function  $g(|\nabla f|) = \exp(-|\nabla f|^2/k^2)$ , and  $|\nabla f|^2$  in (5) is replaced by  $h(|\nabla f|) = 1 - g(|\nabla f|)$ [33]. The GGVF snake possesses improved convergence to long and thin indentations.

## 3. ISAGVF: image structure adaptive gradient vector flow

### 3.1. Proposed ISAGVF model

For the GVF model, we observe the following fact:

$$\begin{aligned} u_x^2 + u_y^2 &= (u_x \ u_y) \begin{pmatrix} u_x \\ u_y \end{pmatrix} = (u_x \ u_y) \begin{pmatrix} 1 & 0 \\ 0 & 1 \end{pmatrix} \begin{pmatrix} u_x \\ u_y \end{pmatrix} \\ &= (\nabla u)^T \begin{pmatrix} 1 & 0 \\ 0 & 1 \end{pmatrix} \nabla u. \end{aligned} \quad (6)$$

Based on this observation, we reformulate the energy function in (4) in the following matrix form:

$$E_{GVF} = \iint \mu \left[ (\nabla u)^T \mathbf{W} \nabla u + (\nabla v)^T \mathbf{W} \nabla v \right] + |\nabla f|^2 |v - \nabla f|^2 dx dy, \quad (7)$$

where  $\mathbf{W}$  is the identity matrix  $\begin{pmatrix} 1 & 0 \\ 0 & 1 \end{pmatrix}$ . It is obvious that this identity matrix induces scalar  $L^2$ -norm and the smoothness constraint in (4) fails to consider the image structure, and finally leads to isotropic diffusion equation (5). Based on this fact, we consider replacing  $\mathbf{W}$  with a matrix  $\mathbf{D}$  related to the image structure so that the GVF vectors can diffuse according to the image structure

adaptively. The new model is named as image structure adaptive gradient vector flow (ISAGVF) and is formulated as follows:

$$E_{ISGVF} = \iint \mu \left[ (\nabla u)^T \mathbf{D} \nabla u + (\nabla v)^T \mathbf{D} \nabla v \right] + |\nabla f|^2 |v - \nabla f|^2 dx dy, \tag{8}$$

where  $\mathbf{D} = \begin{pmatrix} a & b \\ b & c \end{pmatrix}$  is a symmetric and positive semidefinite matrix. The Euler-Lagrange equations for the ISAGVF energy in (8) are as follows:

$$\begin{cases} \mu \operatorname{div}(\mathbf{D} \nabla u) - |\nabla f|^2 (u - f_x) = 0 \\ \mu \operatorname{div}(\mathbf{D} \nabla v) - |\nabla f|^2 (v - f_y) = 0 \end{cases}, \tag{9}$$

where  $\operatorname{div}$  is the divergence operator. A good choice for  $\mathbf{D}$  is the image structure tensor. For image  $\mathbf{I}$ , the image structure reads:

$$\mathbf{S}(\nabla I) = \nabla I (\nabla I)^T = \begin{pmatrix} I_x^2 & I_x I_y \\ I_x I_y & I_y^2 \end{pmatrix}. \tag{10}$$

$\mathbf{S}$  is a symmetric and positive semidefinite matrix. To note, when the image structure  $\mathbf{S}$  is chosen for  $\mathbf{D}$ , Equation (9) happens to be the structure tensor-based diffusion in [59], and we will borrow the strategies there to construct the diffusion tensor  $\mathbf{D}$  from image structure tensor  $\mathbf{S}$ . A previous study [21] adopted the Hessian matrix, but the Hessian matrix is sensitive to noise due to the second order derivatives.

### 3.2. Construction of the diffusion matrix $\mathbf{d}$

In this subsection, we will build the matrix  $\mathbf{D}$  from matrix  $\mathbf{S}$ . Suppose the eigenvectors of  $\mathbf{S}$  are  $\vec{v}_1$  and  $\vec{v}_2$ , the corresponding eigenvalues are  $\lambda_1$  and  $\lambda_2$ ,  $U = (\vec{v}_1, \vec{v}_2)$ , and  $\Lambda = \operatorname{diag}(\lambda_1, \lambda_2)$ , the structure tensor  $\mathbf{S}$  can be decomposed by the principal axis transformation [59], as follows:

$$\mathbf{S}(\nabla I) = U^T \Lambda U. \tag{11}$$

For convenience, the structure tensor  $\mathbf{S}$  is rewritten as follows,

$$\mathbf{S} = \begin{pmatrix} s_{11} & s_{12} \\ s_{12} & s_{22} \end{pmatrix}. \tag{12}$$

Assume that the matrix  $\mathbf{S}$  in (12) has an eigenvalue  $\lambda$  and the corresponding eigenvector  $\vec{v} = (\psi_1, \psi_2)^T$ . According to the linear algebra, we have the following equations:

$$\begin{pmatrix} s_{11} & s_{12} \\ s_{12} & s_{22} \end{pmatrix} \begin{pmatrix} \psi_1 \\ \psi_2 \end{pmatrix} = \lambda \begin{pmatrix} \psi_1 \\ \psi_2 \end{pmatrix}, \tag{13}$$

which is equivalent to:

$$\begin{pmatrix} s_{11} - \lambda & s_{12} \\ s_{12} & s_{22} - \lambda \end{pmatrix} \begin{pmatrix} \psi_1 \\ \psi_2 \end{pmatrix} = 0. \tag{14}$$

The eigenvalues of the matrix  $\mathbf{S}$  in (12) can be determined by the determinant of the left-hand  $2 \times 2$  matrix in (14), which is:

$$\lambda_{1,2} = \frac{1}{2} [s_{11} + s_{22} \pm \sqrt{(s_{11} - s_{22})^2 + 4s_{12}^2}], \tag{15}$$

where  $\lambda_1$  corresponds to the “+” sign in (15). The corresponding eigenvectors  $\vec{v}_1 = (\varphi_1, \varphi_2)^T$  and  $\vec{v}_2 = (\zeta_1, \zeta_2)^T$  take the following forms:

$$\begin{cases} \varphi_1 = \frac{2s_{12}}{\sqrt{(s_{22}-s_{11}+\sqrt{(s_{11}-s_{22})^2+4s_{12}^2})^2+4s_{12}^2}} \\ \varphi_2 = \frac{s_{22}-s_{11}+\sqrt{(s_{11}-s_{22})^2+4s_{12}^2}}{\sqrt{(s_{22}-s_{11}+\sqrt{(s_{11}-s_{22})^2+4s_{12}^2})^2+4s_{12}^2}} \end{cases}, \tag{16}$$

$$\begin{cases} \zeta_1 = \frac{2s_{12}}{\sqrt{(s_{22}-s_{11}-\sqrt{(s_{11}-s_{22})^2+4s_{12}^2})^2+4s_{12}^2}} \\ \zeta_2 = \frac{s_{22}-s_{11}-\sqrt{(s_{11}-s_{22})^2+4s_{12}^2}}{\sqrt{(s_{22}-s_{11}-\sqrt{(s_{11}-s_{22})^2+4s_{12}^2})^2+4s_{12}^2}} \end{cases}, \tag{17}$$

Since  $\mathbf{S}$  has the form in (10), following the discussion above, we can get the following results:

$$\begin{cases} \lambda_1 = |\nabla I|^2 \\ \vec{v}_1 = (I_x/|\nabla I|, I_y/|\nabla I|)^T \end{cases}, \tag{18}$$

$$\begin{cases} \lambda_2 = 0 \\ \vec{v}_2 = (-I_y/|\nabla I|, I_x/|\nabla I|)^T \end{cases} \tag{19}$$

It is easy to verify that the eigenvector  $\vec{v}_1$  is parallel to the gradient vector, whereas  $\vec{v}_2$  is orthogonal. The eigenvalues  $\lambda_1$  and  $\lambda_2$  can be used as descriptors of local structure [59]; for instance, constant areas are characterized by  $\lambda_1 = \lambda_2 = 0$  and straight edges give  $\lambda_1 \gg \lambda_2 = 0$ .

However, the image structure tensor  $\mathbf{S}$  cannot be directly employed for  $\mathbf{D}$  as  $\lambda_2 = 0$  means that the vectors diffuse always merely along the gradient directions, therefore destroying the edges. To construct the reasonable diffusion tensor  $\mathbf{D}$ , we choose the orthonormal eigenvectors of  $\mathbf{S}$ , i.e.,  $\vec{v}_1$  and  $\vec{v}_2$ , as the eigenvectors of  $\mathbf{D}$ , while the eigenvalues of  $\mathbf{D}$  denoted by  $\omega_1$  and  $\omega_2$  are different from those of  $\mathbf{S}$ , which depends on the goal of application [59]. Then,  $\mathbf{D}$  can be constructed as:

$$\mathbf{D} = (\vec{v}_1 \quad \vec{v}_2)^T \begin{pmatrix} \omega_1 & 0 \\ 0 & \omega_2 \end{pmatrix} (\vec{v}_1 \quad \vec{v}_2). \tag{20}$$

Using (16) and (17),  $\mathbf{D}$  is finally represented as:

$$\mathbf{D} = \begin{pmatrix} \frac{1}{2}(\omega_1 + \omega_2 + \frac{(\omega_2 - \omega_1)(s_{22} - s_{11})}{\sqrt{(s_{11} - s_{22})^2 + 4s_{12}^2}}) & \frac{(\omega_1 - \omega_2)s_{12}}{\sqrt{(s_{11} - s_{22})^2 + 4s_{12}^2}} \\ \frac{(\omega_1 - \omega_2)s_{12}}{\sqrt{(s_{11} - s_{22})^2 + 4s_{12}^2}} & \frac{1}{2}(\omega_1 + \omega_2 - \frac{(\omega_2 - \omega_1)(s_{22} - s_{11})}{\sqrt{(s_{11} - s_{22})^2 + 4s_{12}^2}}) \end{pmatrix}. \tag{21}$$

The performances of the proposed ISAGVF model mostly depend on the choice of the eigenvalues  $\omega_1$  and  $\omega_2$ .  $\omega_1$  represents the diffusion coefficient parallel to the gradient vector, while  $\omega_2$  is the diffusion coefficient along the edges. The choice of  $\omega_1$  and

$\omega_2$  conforms to the following criterion [59]: a higher value implies that the diffusion in the direction of the corresponding eigenvector will be encouraged. In the proposed model,  $\omega_1$  and  $\omega_2$  take the following form for the application on hand:

$$\begin{cases} \omega_1 = \frac{1}{1 + \left(\frac{|\nabla I|}{K}\right)^2}, \\ \omega_2 = 1 \end{cases}, \quad (22)$$

where  $K$  is the gradient threshold of a given image. The settings of parameter  $K$  will be further elucidated in Section 4. It can be observed that

- (1) For  $|\nabla I| \rightarrow \infty$ , i.e., the edges,  $\omega_1(|\nabla I|)/\omega_2(|\nabla I|) = 1/(1 + (|\nabla I|/K)^2) \rightarrow 0$ , ISAGVF prefers diffusing along the edge. As a result, the edge can be preserved, and the noise can be removed;
- (2) For  $|\nabla I| \rightarrow 0$ , i.e., the homogeneous region,  $\omega_1(|\nabla I|) = \omega_2(|\nabla I|) = 1 > 0$ , diffusing is isotropic, and the noise can be reduced accordingly.

In this way, the proposed ISAGVF diffuses adaptively according to the image structure, which would help the snake to preserve weak edges and enter narrow and deep concavities and even complex structures. The details of numerical implementation have been described by [59].

## 4. Experimental results and discussion

In this section, we evaluate the performance of the ISAGVF snake in terms of capture range, weak edge preservation, and narrow and deep concavity convergence, as well as complex structure convergence, and make comparisons with several popular GVF-like models, including the GVF [32], GGVF [33], NGVF [44], ILGVF [39], VEF [42], and BVF [43]. The parameters for all snakes in our experiments are  $\alpha = 0.1$ ,  $\beta = 0.1$ , and time step  $\tau = 0.5$ , and the image intensity is normalized to range  $[0, 1]$ . For an image of size  $M \cdot N$ , the iteration for the calculation of all GVF-like models is  $\sqrt{M \cdot N}$ , and the time step is  $1 \ll 1/(4\mu)$ . To obtain a large capture range and more regular force field, the parameter  $\mu$  for GVF, NGVF, ILGVF is 0.2, and 0.1 for the ISAGVF, and  $K = 0.5$  for GGVF,  $\omega = 1.0$  for BVF, and the convolution kernel size for the VEF model is a quarter of the image size. Parameter  $K$  for the ISAGVF is a constant that determines the contrast of the edges to be preserved and it is 0.1, unless otherwise stated [59]. As different models adopt different mechanisms, the same parameter may not be optimal for different models; as a result, we adopted different values for some parameters in different models so that the performances of different models are optimal.

### 4.1. Common properties: enlarged capture range and initialization insensitivity

To confirm that the proposed model has a sufficient capture range, the usually employed room and U-shape images are enlarged to a size of  $128 \times 128$  pixels, while the size of both objects is fixed. The enlarged images are shown in Figure 1A, the corresponding

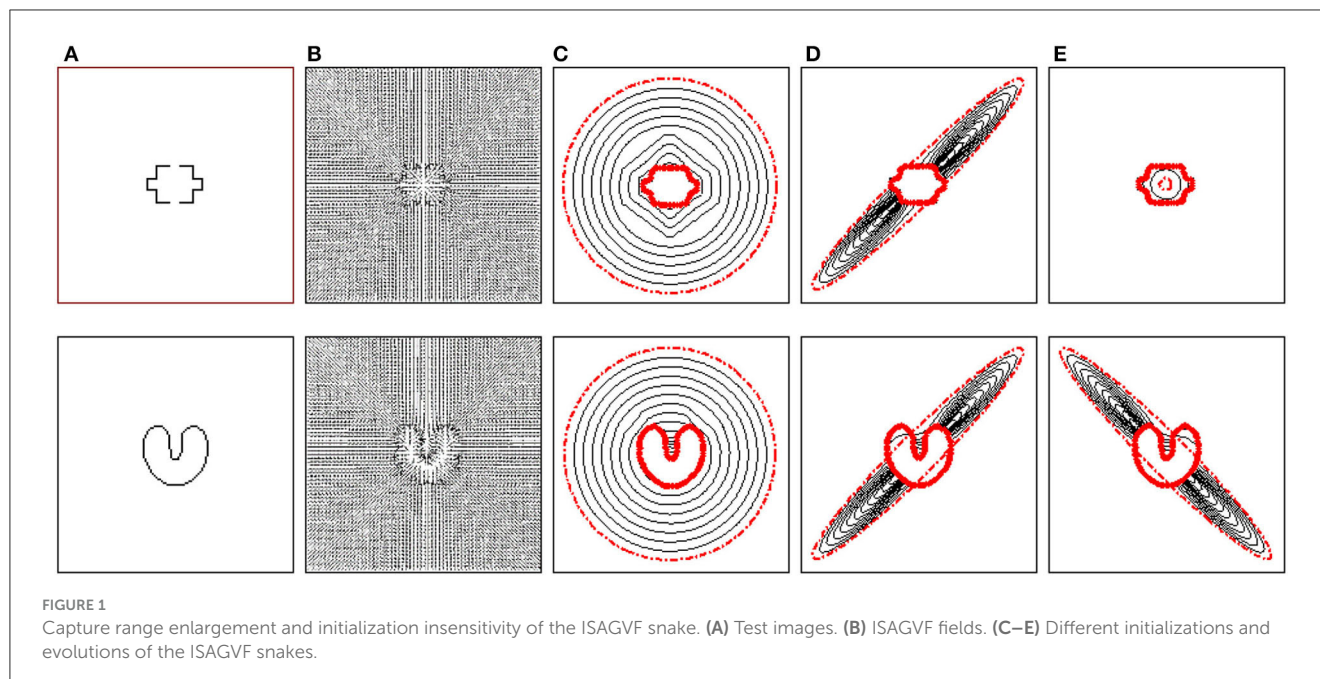
ISAGVF fields are shown in Figure 1B, and the initial contours and the evolution results of the proposed ISAGVF snake model for three different objects are shown in Figures 1C–E, respectively. Although the initializations are placed far away, across or inside the objects, the ISAGVF snakes converge to the true boundaries regularly; this fact manifests that the proposed ISAGVF snake is insensitive to initialization and has a large capture range.

### 4.2. Narrow and deep concavity convergence

It is well-known that the GVF snake can converge to U-shape concavity, but when the concavity becomes narrower and deeper, it is very difficult for the GVF snake to converge. However, the proposed ISAGVF snake possesses great power for this issue as the ISAGVF model takes into account the image structure. Figure 2 shows three testing concavity images. The first one is an “E”-shaped image with an upper concavity width of 3 pixels and a depth of 35 pixels and the bottom one has a width of 3 pixels and a depth of 40 pixels. One can see that the BVF snake and the proposed ISAGVF snake dived into both concavities successfully, but the others failed. Another interesting observation is that the GGVF snake succeeded in a concavity with a depth of 35 pixels but failed in the concavity with a depth of 40 pixels; the reason behind this fact is that the GGVF model is just a weighted version of the GVF model (both are isotropic). The second one is a “T”-shaped image with a horizontal concavity with a width of 5 pixels and length of 40 pixels, and a vertical concavity with a width of 3 pixels and depth of 40 pixels. It was observed that the GGVF, NGVF, BVF, and ISAGVF snakes converged to the horizontal concavity, whereas just the ISAGVF snake succeeded in the vertical one, although the vertical concavity is narrower. For the cross image in the third row, the four concavities each have a width of 3 pixels and depth of 50 pixels. It was observed that just the NGVF and ISAGVF snakes dived into the concavities successfully; the GVF, GGVF, and VEF snakes were halfway from converging in the concavities, while the ILGVF and BVF snakes were merely on the ready line. From these results, the performance of the ISAGVF snake with respect to concavity convergence is verified.

### 4.3. Weak edge preserving

A weak edge often appears in images and it is nuisance for image segmentation, especially for snake-based methods when there are some strong edges nearby. Figure 3A shows two examples. The first one is an image of two disks (see the upper panel). The upper-left edge of the outer disk is blurred and weak and the neighboring edge of the inner one is strong. The second example is an image composed of three gray values (0, 255, and 245, see the bottom panel). The edge between the region of gray value 0 and that of gray value 255 is strong, whereas the edge between the region of gray value 255 and that of gray value 245 is weak. Both edge maps are shown in Figure 3B, from which one can see that the weak edges in both examples are almost invisible, and the snake contours are used to being attracted by the strong



edges nearby. The convergence results of (C) GVF, (D) GGVF, (E) NGVF, (F) ILGVF, (G) BVF, (H) VEF, and (I) ISAGVF snakes are shown in [Figures 3C–I](#), respectively. As expected, all the models employed for comparison failed to capture the weak edge, while the proposed ISAGVF snake resisted the lure from the strong edge and caught the weak edge successfully. To note, the ILGVF snake expanded the initial contour slightly as the initialization was not in the territory of the force field, although the initial contour touched the weak edge. By contrast, the proposed ISAGVF snake dealt with this issue gracefully thanks to taking into account the image structure. In these experiments, the parameters were  $K = 0.01$  for the ISAGVF model.

#### 4.4. Complex structure convergence

It is well-known that the GVF snake can converge to the U-shape concavity; however, when the concavity is complex, it remains a challenge for the GVF-like methods. The reason behind this is that complex structures may make forces computed from their gradient have different directions, thus making the snake contour stop at an unexpected position. In this subsection, we present six examples with various characteristics to illustrate that the proposed ISAGVF snake has a great advantage in this respect as the ISAGVF model takes the image structure into account. [Figure 4](#) shows the results. The first example is the 3-shape, which has two concavities. The GVF, GGVF, and NGVF stopped at the gate of the concavities, and the ILGVF snake tried to enter the concavities but failed, although the initial contour was very close to the object. After a period of wandering, the BVF snake entered the lower concavity but could not do anything for the upper concavity. By contrast, the VEF and ISAGVF snakes successfully dived into the two concavities. For the other five examples in [Figure 4](#), only the ISAGVF snake succeeded in converging to each concavity; all the

other models failed at all concavities. The great superiority of the ISAGVF snake in taking the image structure into account can be observed from these examples.

#### 4.5. Real images

The proposed ISAGVF snake was also applied to some real images to verify its superiority. In these cases, we had to cope with intensity inhomogeneity, noise, and weak edges neighbored by strong ones. Hence,  $K$  was chosen as 0.01 for the proposed ISAGVF. The image in the [Figure 5](#) is an echocardiographic image of the left ventricle, where the snake contour could be harassed by intensity inhomogeneity, noise, and weak edges. The image is smoothed with a Gaussian filter of a standard deviation of 3 before the edge map was derived. One can see that the GVF and VEF snakes leaked out in both upper and lower areas and the other two also converged to an incorrect position. By contrast, the proposed ISAGVF model stuck to the desired edges. [Figure 6](#) presents the results of a vessel with many branches. To derive the edge map, the image is preprocessed with a Gaussian filter with a standard deviation of 1. With the same initialization, only the ISAGVF snake extracted the boundary successfully, while others blocked the way to some branches.

The image in [Figure 7](#) is a person holding up a stick on a horse. The difficulties of this example reside in the concave region between the person and the stick and the neck and the chin, as well as the tail and the leg of the horse, as pointed out by the three red arrows in [Figure 7A](#). The person with the stick is cropped to show the close-up of the converged result of each method. It can be observed that just the GGVF and ISAGVF snakes can cope with the concavity between the tail and the leg of the horse; the GGVF model takes the image structure into account to some degree as it adopts the edge map as weight, while the ISAGVF model takes the image structure into account in the diffusion process. Just

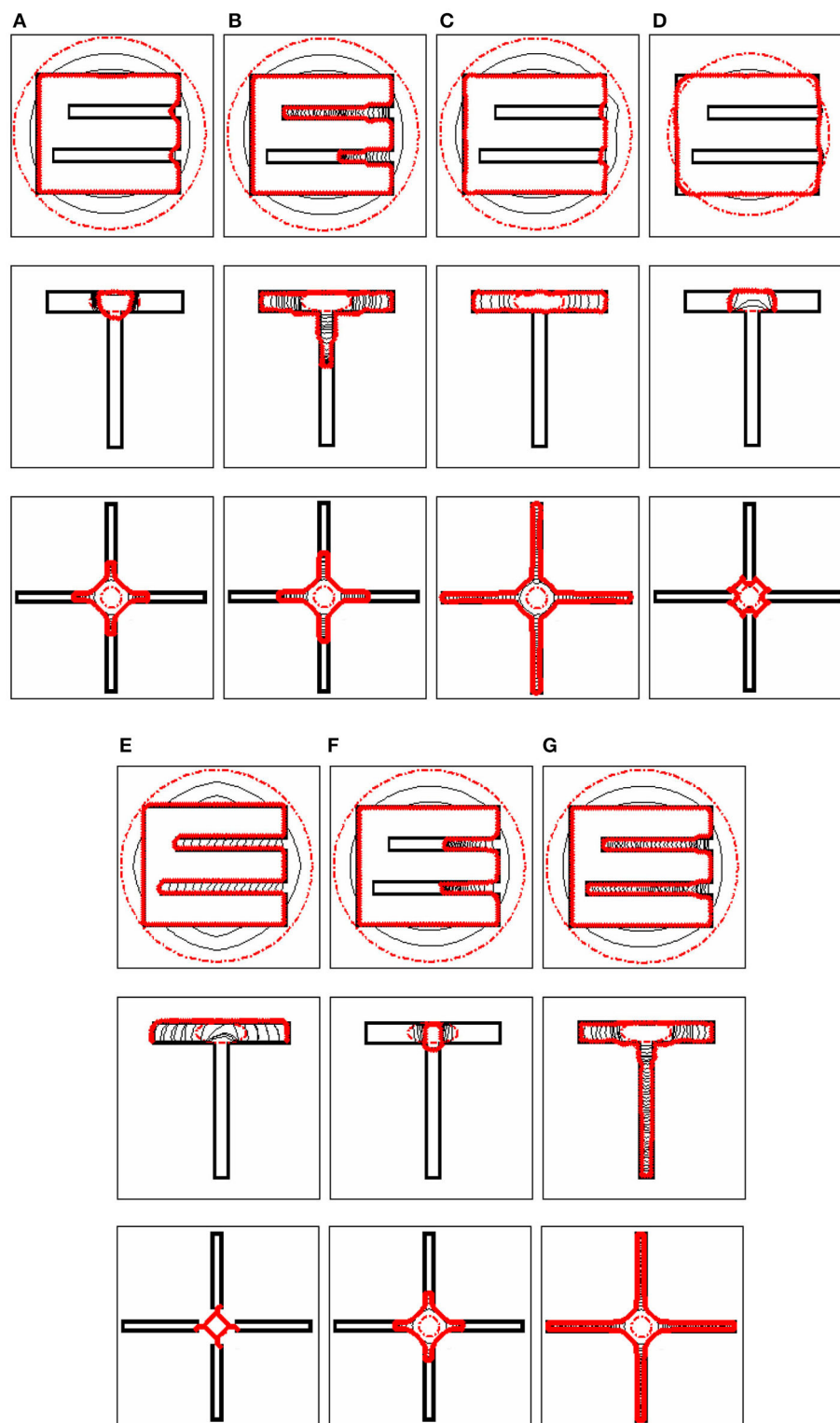


FIGURE 2

Concavity convergence of the snakes. The first testing image is an "E"-shaped image with an upper concavity width of 3 pixels and depth of 35 pixels and the bottom concavity has a width of 3 pixels and length of 40 pixels. The second image is a "T"-shaped image with a horizontal concavity with a width of 5 pixels and depth of 40 pixels, and a vertical concavity with a width of 3 pixels and depth of 40 pixels. The third one is a cross-shaped image with four concavities each with a width of 3 pixels and depth of 50 pixels. The convergence results of (A) GVF, (B) GGVF, (C) NGVF, (D) ILGVF, (E) BVF, (F) VEF, and (G) ISAGVF snakes are shown as solid red lines.

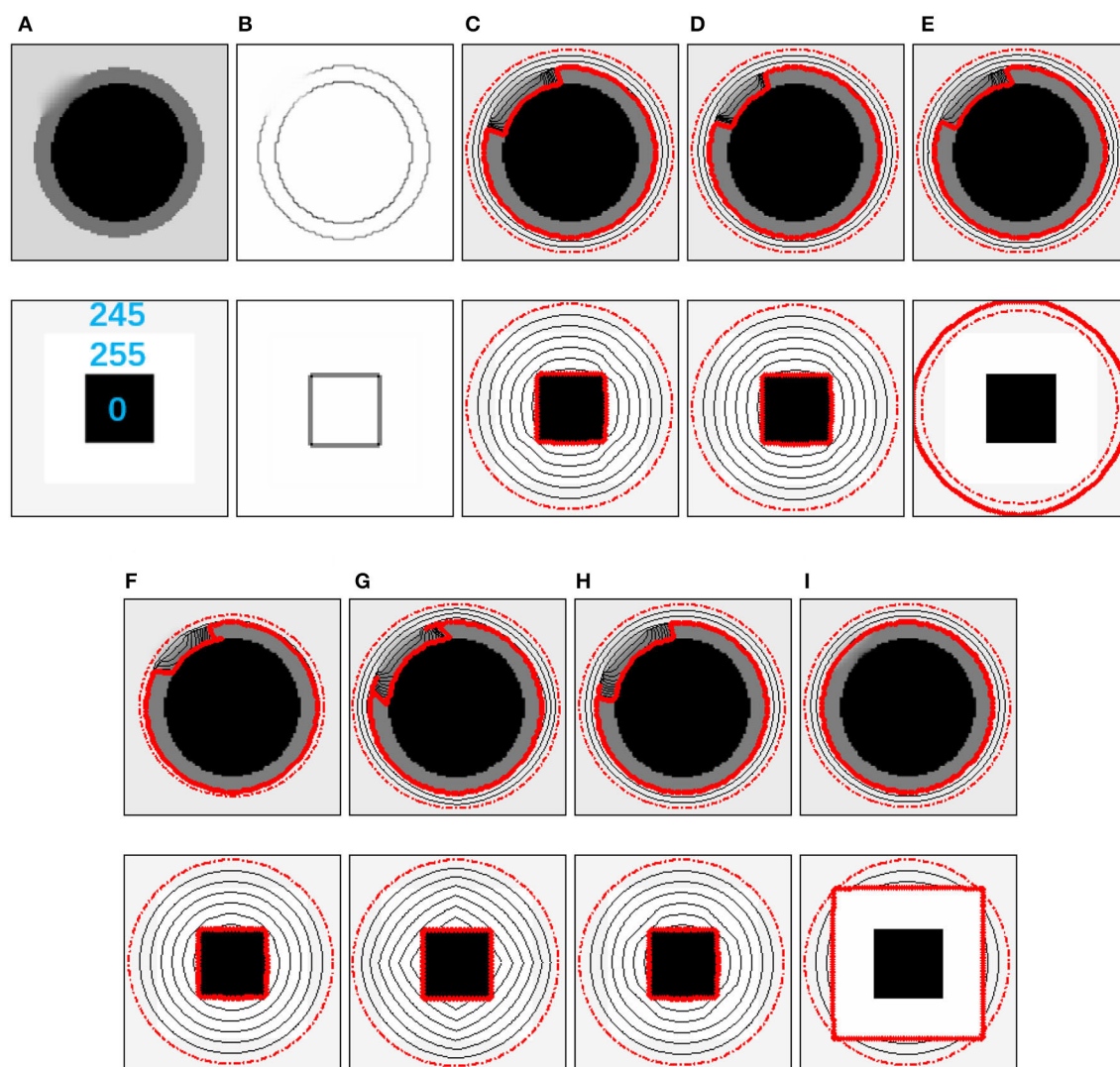


FIGURE 3

Weak edge preserving demonstrations. There are two weak edge examples. (A) The test images. (B) Edge maps. The convergence results of (C) GVF, (D) GGVF, (E) NGVF, (F) ILGVF, (G) BVF, (H) VEF, and (I) ISAGVF snakes are shown as solid red lines, and the dash-point circles in red are the initial contours.

for this reason, only the proposed ISAGVF snake can successfully converge to the other two concave regions. When the close-ups of the converged results of each method are inspected, the GVF snake cannot preserve the head of the person and the thin stick (see Figure 7C), while the GGVF snake can correctly capture the head and the thin stick; however, it failed to converge to the concave region (see Figure 7D). In the case of NGVF, the diffusion continues in the normal direction and the convergence result is irregular (Figure 7E). The result of the BVF snake in Figure 7F shows that it can capture the head of the person correctly but cannot capture the thin stick and cannot enter the concavity. Although the VEF snake can extract the head of the person, it fails to catch the stick (see Figure 7G). In addition, the proposed ISAGVF snake can catch the thin stick and enter the concave region successfully (see Figure 7H). The superiority of the ISAGVF snake by taking the image structure into account is demonstrated thoroughly.

Figure 8 shows an image of a USB flash disk on the back of a hand. The disk yields a strong edge near the sleeve opening that may probably attract the snake contour. The results show that only the proposed ISAGVF snake can resist the lure of the strong edge and correctly capture the shape of the hand. Figure 9 shows more results of the ISAGVF snake on real images, and the results are satisfactory.

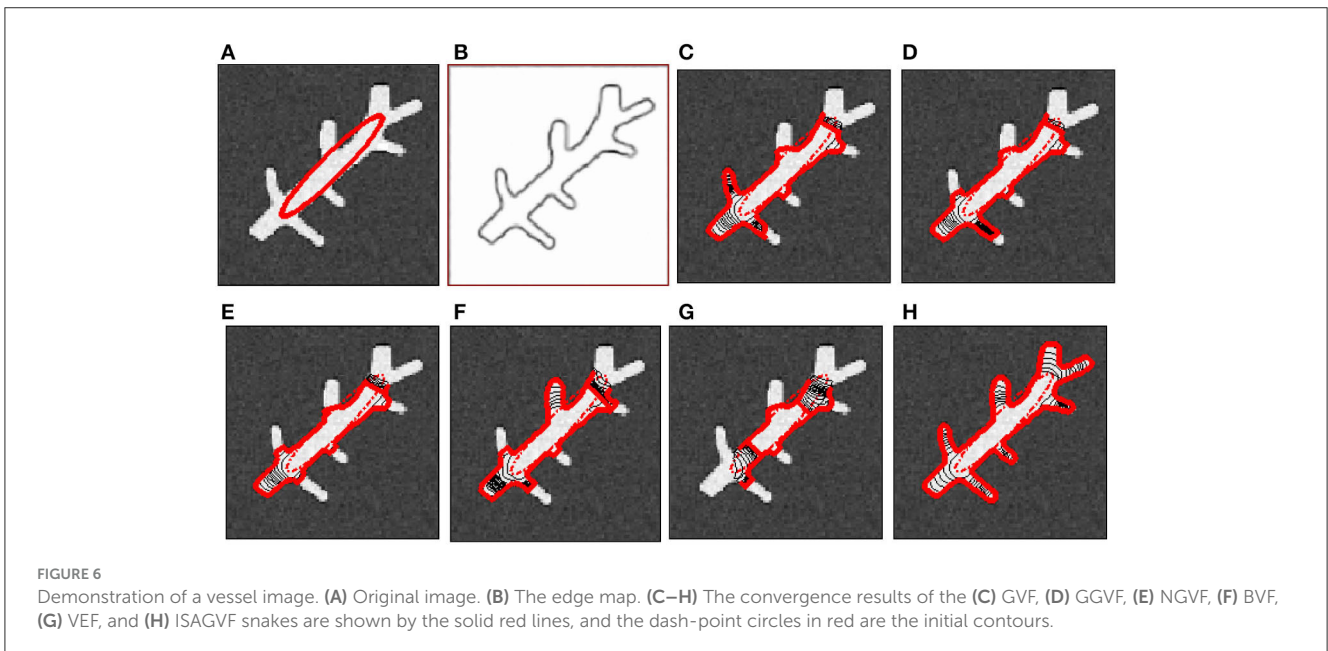
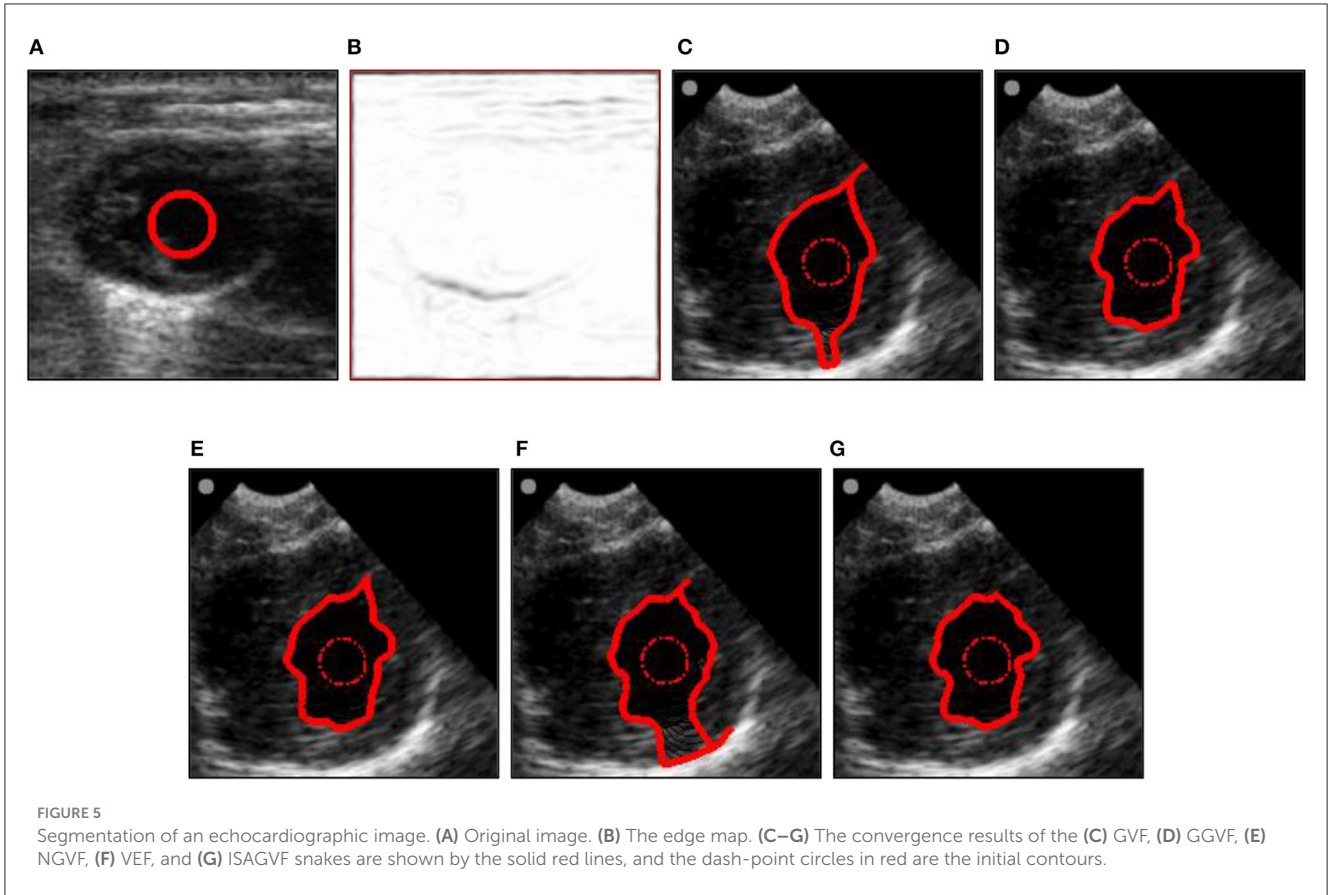
#### 4.6. Discussion

As we know, it is contradictory to preserve weak edges and smooth noise simultaneously for the external force of the snake model. Parameter  $K$  in the proposed ISAGVF model serves as the gradient threshold, the value of which depends on the preservation of the magnitude of the gradient of the weak edge. Through a



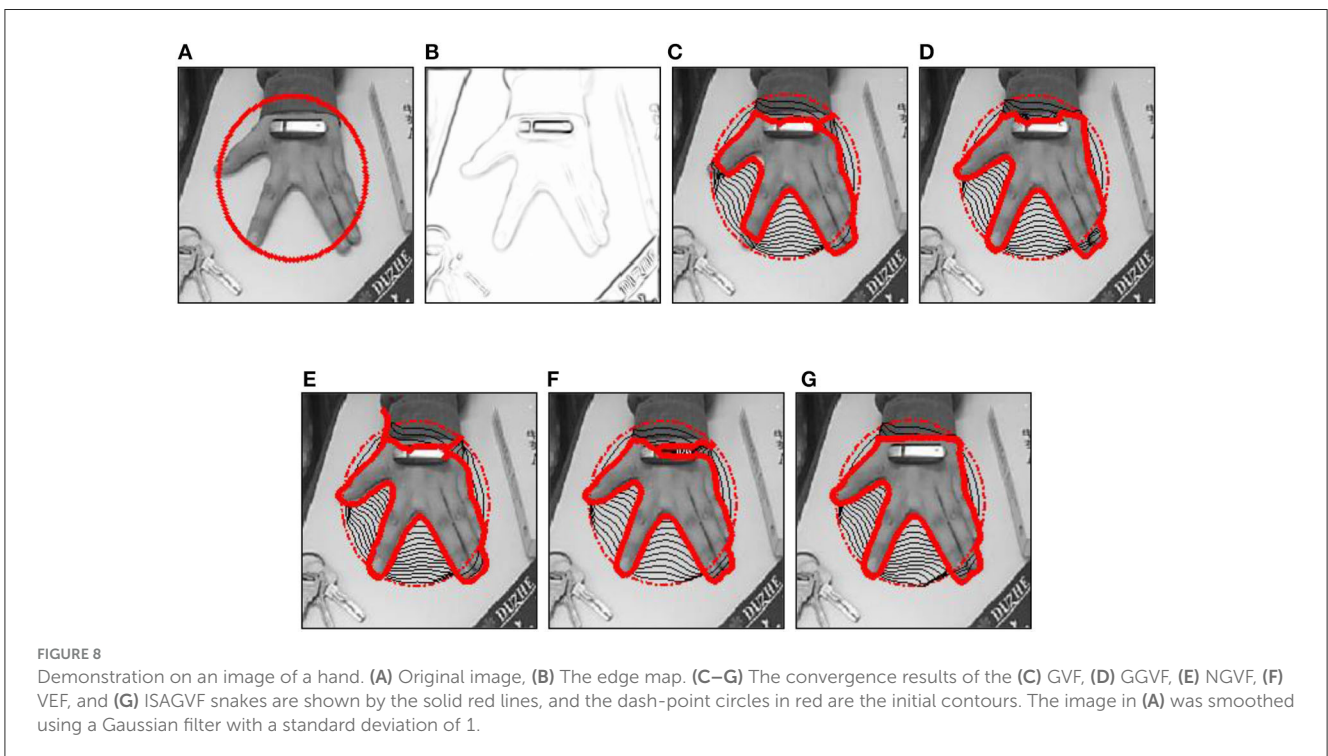
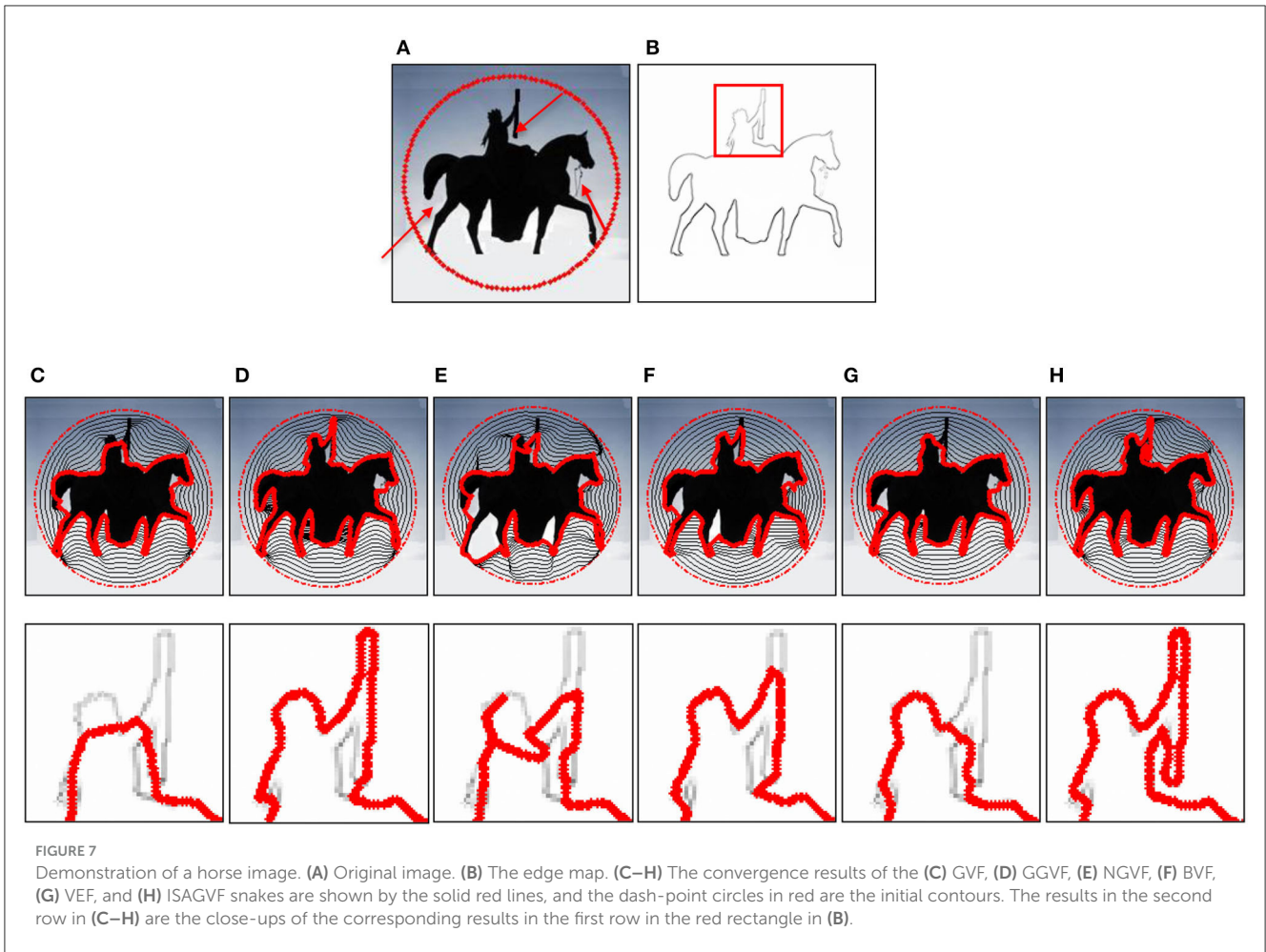
FIGURE 4

Demonstration and comparison of complex concavity convergence. The convergence results of (A) GVF, (B) GGVF, (C) NGVF, (D) ILGVF, (E) BVF, (F) VEF, and (G) ISAGVF snakes are shown by the solid red lines, and the dash-point circles in red are the initial contours.



lot of tests, we found that, for the vast majority of the images,  $K$  ranges from 0.01 to 0.5. At the same time, a large  $K$  can also suppress noise to some degree; if the image has a lot of noise, we can choose a relatively larger  $K$  to suppress it without disturbing

the edge. As shown in the top row of [Figure 10](#), the snake model stuck in the concavity due to noise with the smallest  $K$ . However, as  $K$  increases, it resists noise more and becomes better at entering concavities. Additionally, when there are some weak edges in the



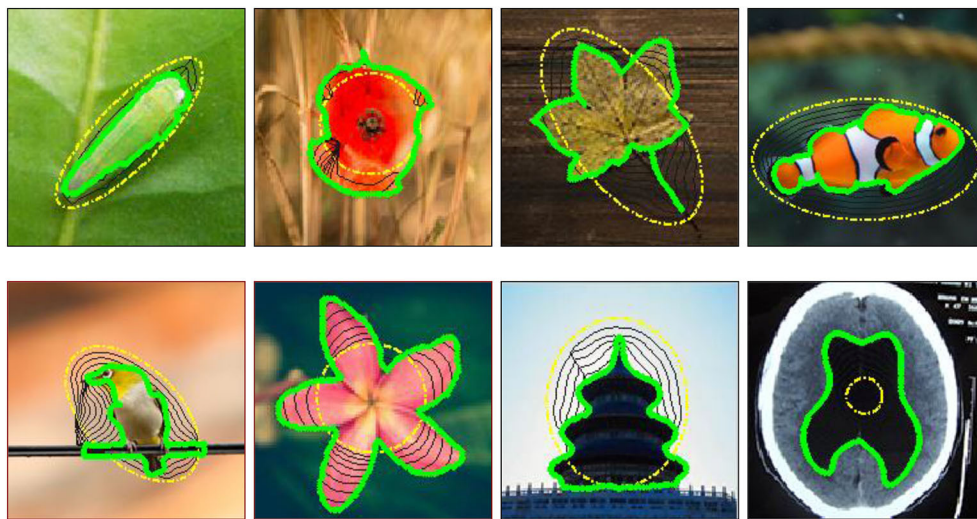


**FIGURE 9**  
 More results of the proposed ISAGVF snake on real images. The dash-point lines in yellow are the initial contours and the solid green lines are the convergence results.

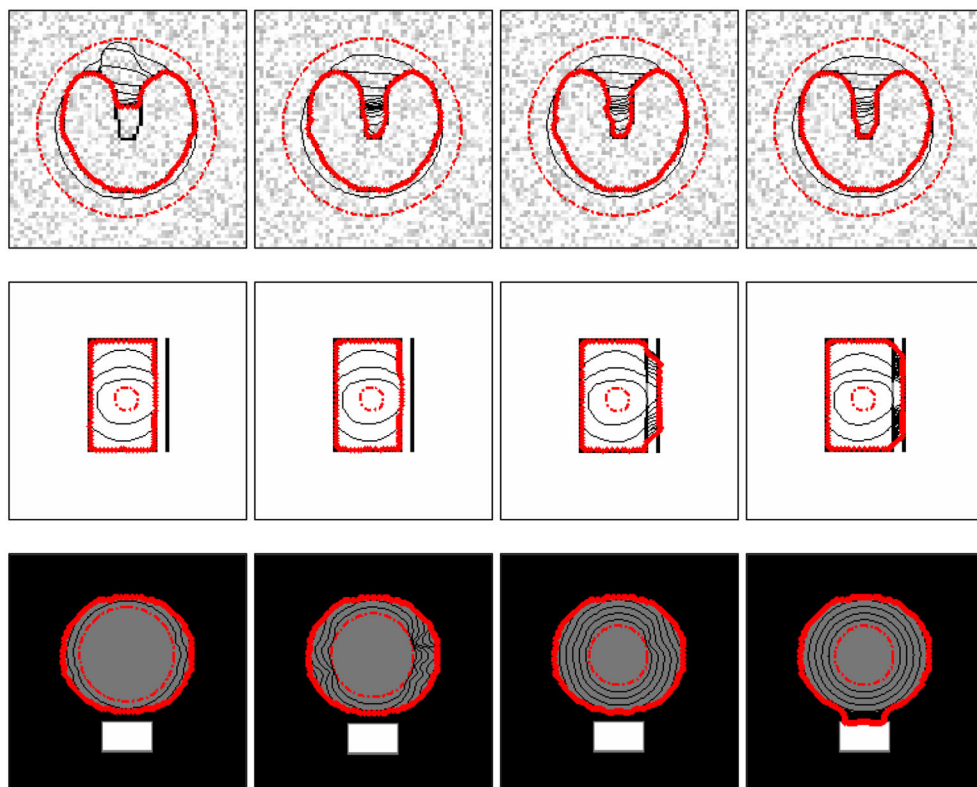


**FIGURE 10**  
 Test of the parameters  $K$  and  $\mu$ . Top row: the segmentation results of images with noise. Second row: the segmentation results of images where there are strong edges nearby weak edges. The  $\mu$  is 0.2 and  $K$ -values from left to right are 0.01, 0.05, 0.1, and 0.5, respectively. For the third row,  $K$  is 0.1 and  $\mu$  values from left to right are 0.001, 0.02, 0.1, and 0.2, respectively.

image, we should make it smaller to preserve the edge of the object. The results in the bottom row of Figure 10 demonstrate our analysis, i.e., a  $K$  that is too large will lead to weak boundary

leakage. Parameter  $\mu$  mainly controls the diffusion degree of the external force field in homogeneous region. The larger  $\mu$  is, the larger the diffusion degree of the external force field. In other words,

a large  $\mu$  helps to smooth noise and results in a large capture range. Therefore,  $K$  and  $\mu$  are closely linked. As we can see from the third row in Figure 10, when  $\mu$  takes a smaller value, the capture range of the vector field is not enough, and thus the initialization needs to be close to the boundary of the object, but at the same time the weak edge can be protected. As  $\mu$  increases, the capture range becomes increasingly larger, and finally, the strong edge may attract the weak edge. In short, the parameters  $K$  and  $\mu$  can change interactively to smooth noise, preserve weak edges, and extend the capture range.

## 5. Conclusion

A novel external force called image structure adaptive gradient vector flow (ISAGVF) is proposed for active contours. Given that the smoothness constraint of the GVF model does not take the image structure into account, the smoothness constraint was rewritten in a matrix form and the image structure tensor was introduced into the smoothness constraint, such that the proposed ISAGVF model behaves in an anisotropic manner. A simple and effective method was also adopted to construct the diffusion tensor from the image structure tensor. Experimental results on both synthetic and real images showed that the ISAGVF snake is superior to other popular models in terms of weak edge preservation, deep concavity entering, and some complex convergence.

## Data availability statement

The original contributions presented in the study are included in the article/supplementary material, further inquiries can be directed to the corresponding authors.

## References

1. Kass M, Witkin A, Terzopoulos D. Snake: active contour models. *Int J Comput Vis.* (1988) 1:321–31. doi: 10.1007/BF00133570
2. Caselles V, Catta F, Coll T, Dibos F. A geometric model for active contours. *Numer Math.* (1993) 66:1–31. doi: 10.1007/BF01385685
3. Gui L, Li C, Yang X. Medical image segmentation based on level set and isoperimetric constraint. *Phys Med.* (2017) 42:162–73. doi: 10.1016/j.ejmp.2017.09.123
4. Zhao Y, Guo S, Luo M, Shi X, Bilello M, Zhang S, et al. level set method for multiple sclerosis lesion segmentation. *Magn Reson Imaging.* (2018) 49:94–100. doi: 10.1016/j.mri.2017.03.002
5. Khadidos A, Sanchez V, Li C-T. Weighted level set evolution based on local edge features for medical image segmentation. *IEEE Transact Image Process.* (2017) 26:1979–91. doi: 10.1109/TIP.2017.2666042
6. Ali H, Sher A, Saeed M, Rada L. An active contour image segmentation model with de-hazing constraints. *IET Image Process.* (2020). 14:921–8. doi: 10.1049/iet-ipr.2018.5987
7. Liu G, Zou J. Level set evolution with sparsity constraint for object extraction. *IET Image Process.* (2018) 12:1413–22. doi: 10.1049/iet-ipr.2017.0939
8. Karn PK, Biswal B, Samantaray SR. Robust retinal blood vessel segmentation using hybrid active contour model. *IET Image Process.* (2019) 13:440–50. doi: 10.1049/iet-ipr.2018.5413
9. Chen Y, Zhang J, Mishra A, Yang J. Image segmentation and bias correction via an improved level set method. *Neurocomputing.* (2011) 74:3520–30. doi: 10.1016/j.neucom.2011.06.006
10. Wang Y, Wang H, Xu Y. Texture segmentation using vector-valued Chan-Vese model driven by local histogram. *Comp Elect Eng.* (2013) 39:1506–15. doi: 10.1016/j.compeleceng.2013.03.017
11. Wu H, Appia V, Yezzi A. Numerical conditioning problems and solutions for nonparametric IID statistical active contours. *IEEE Transact Pattern Anal Mach Intell.* (2013) 35:1298–311. doi: 10.1109/TPAMI.2012.207
12. Kim W, Kim C. Active contours driven by the salient edge energy model. *IEEE Transact Image Process.* (2012) 22:1667–73. doi: 10.1109/TIP.2012.2231689
13. Wang W, Wang Y, Wu Y, Lin T, Li S, Chen B. Quantification of full left ventricular metrics via deep regression learning with contour-guidance. *IEEE Access.* (2019) 7:47918–28. doi: 10.1109/ACCESS.2019.2907564
14. Shen W, Xu W, Zhang H, Sun Z, Ma J, Ma X, et al. Automatic segmentation of the femur and tibia bones from X-ray images based on pure dilated residual U-Net. *Inverse Prob Imaging.* (2021) 15:1333–46. doi: 10.3934/ipi.2020057
15. Zhao C, Xiang S, Wang Y, Cai Z, Shen J, Zhou S, et al. Context-aware network fusing transformer and V-Net for semi-supervised segmentation of 3D left atrium. *Expert Syst Appl.* (2023) 214:119105. doi: 10.1016/j.eswa.2022.119105
16. Chen LC, Papandreou G, Kokkinos I, Murphy K, Yuille AL. DeepLab: semantic image segmentation with deep convolutional nets, atrous convolution, and fully connected CRFs. *IEEE Trans Pattern Anal Mach Intell.* (2018) 40:834–48. doi: 10.1109/TPAMI.2017.2699184
17. Zhang H, Zhang W, Shen W, Li N, Chen Y, Li S, et al. Automatic segmentation of the left ventricle from MR images based on nested U-Net with dense block. *Biomed Signal Process Control.* (2021) 68:102684. doi: 10.1016/j.bspc.2021.102684

## Author contributions

DW: Methodology, Software, Writing—original draft. XD: Funding acquisition, Investigation, Resources, Validation, Visualization, Writing—review and editing. WL: Visualization, Data curation, Methodology, Project administration, Writing—original draft. YW: Conceptualization, Funding acquisition, Investigation, Supervision, Writing—review and editing. All authors contributed to the article and approved the submitted version.

## Funding

The author(s) declare financial support was received for the research, authorship, and/or publication of this article. This study was supported in part by the National Science Foundation of China (NSFC) (61976241).

## Conflict of interest

The authors declare that the research was conducted in the absence of any commercial or financial relationships that could be construed as a potential conflict of interest.

## Publisher's note

All claims expressed in this article are solely those of the authors and do not necessarily represent those of their affiliated organizations, or those of the publisher, the editors and the reviewers. Any product that may be evaluated in this article, or claim that may be made by its manufacturer, is not guaranteed or endorsed by the publisher.

18. Uhlmann V, Fageot J, Unser M. Hermite snakes with control of tangents. *IEEE Trans Image Process.* (2016) 25:2803–16. doi: 10.1109/TIP.2016.2551363
19. Delgado-Gonzalo R, Uhlmann V, Schmitter D, Unser M. Snakes on a plane: A perfect snap for bioimage analysis. *IEEE Signal Processing Mag.* (2015) 32:41–8. doi: 10.1109/MSP.2014.2344552
20. Zareei A, Karimi A. Liver segmentation with new supervised method to create initial curve for active contour. *Comput Biol Med.* (2016) 75:139–50. doi: 10.1016/j.combiomed.2016.05.009
21. Qian Q, Cheng K, Qian W, Deng Q, Wang Y. Image segmentation using active contours with hessian based gradient vector flow external force. *Sensors.* (2022) 22:4956. doi: 10.3390/s22134956
22. Zhang Z, Duan C, Lin T, Zhou S, Wang Y, Gao X, et al. A novel external force for active contour based image segmentation. *Inf Sci.* (2020) 506:1–18. doi: 10.1016/j.ins.2019.08.003
23. Song TH, Sanchez V, Eidaly H, Rajpoot NM. Dual-channel active contour model for megakaryocytic cell segmentation in bone marrow trephine histology images. *IEEE Trans Biomed Eng.* (2017) 64:2913–23. doi: 10.1109/TBME.2017.2690863
24. Berenguer-Vidal R, Verdú-Monedero R, Morales-Sánchez J, Sellés-Navarro I, Del Amor R, García G, et al. Automatic segmentation of the retinal nerve fiber layer by means of mathematical morphology and deformable models in 2D optical coherence tomography imaging. *Sensors.* (2021) 21:8027. doi: 10.3390/s21238027
25. Maneerat A, Visitsattapong S, Pintavirooj C. Bone mineral density screening system using CMOS-sensor X-ray detector. *Sensors.* (2021) 21:7148. doi: 10.3390/s21217148
26. Jia D, Zhang C, Wu N, Guo Z, Ge H. Multi-layer segmentation framework for cell nuclei using improved GVF Snake model, Watershed, and ellipse fitting. *Biomed Signal Process Control.* (2021) 67:102516. doi: 10.1016/j.bspc.2021.102516
27. Yu S, Lu Y, Molloy D. A dynamic-shape-prior guided snake model with application in visually tracking dense cell populations. *IEEE Transact Image Process.* (2019) 28:1513–27. doi: 10.1109/TIP.2018.2878331
28. Zhao SH Li G, Zhang W, Gu J. Automatic intima-media border segmentation on ultrasound image sequences using a Kalman filter snake. *IEEE Access.* (2018) 6:40804–10. doi: 10.1109/ACCESS.2018.2856244
29. Manno-Kovacs A. Direction selective contour detection for salient objects. *IEEE Transact Circ Syst Video Technol.* (2018) 29. doi: 10.1109/TCSVT.2018.2804438
30. Cohen LD. On active contour models and balloons. *CVGIP Image Understand.* (1991) 53:211–8. doi: 10.1016/1049-9660(91)90028-N
31. Cohen LD, Cohen I. Finite-element methods for active contour models and balloons for 2-D and 3-D images. *IEEE Trans Pattern Anal Mach Intell.* (1993) 15:1131–47. doi: 10.1109/34.244675
32. Xu C, Prince J. Snakes, shapes and gradient vector flow. *IEEE Trans Image Process.* (1998) 17:359–69. doi: 10.1109/83.661186
33. Xu C, Prince JL. Generalized gradient vector flow external forces for active contours. *Signal Process.* (1998) 71:131–9. doi: 10.1016/S0165-1684(98)00140-6
34. Qin L, Zhu C, Zhao Y, Bai H, Tian H. Generalized gradient vector flow for snakes: new observations, analysis, and improvement. *IEEE Transact Circ Syst Video Technol.* (2013) 23:883–97. doi: 10.1109/TCSVT.2013.2242554
35. Wang Y, Jia Y, Liu L. Harmonic gradient vector flow external force for snake model. *IEE Electron Lett.* (2008) 44:105–7. doi: 10.1049/el:20081650
36. Wang Y, Jia Y. Segmentation of the left ventricle from cardiac MR Images based on degenerated minimal surface diffusion and shape priors. In: *ICPR2006*. Hong Kong, p. 671–674.
37. Wu Y, Wang Y, Jia Y. Adaptive diffusion flow active contours for image segmentation. *Comp Vis Image Understand.* (2013) 117:1421–35. doi: 10.1016/j.cviu.2013.05.003
38. Ray N, Acton ST. Motion gradient vector flow: an external force for tracking rolling leukocytes with shape and size constrained active contours. *IEEE Trans Med Imaging.* (2004) 23:1466–78. doi: 10.1109/TMI.2004.835603
39. Guillot L, Le Guyader C. Extrapolation of vector fields using the infinity laplacian and with applications to image segmentation. *Scale Space Variat Methods Comp Vis.* (2009) 5567:87–99. doi: 10.1007/978-3-642-02256-2\_8
40. Wang Y, Liu L, Zhang H, Cao Z, Lu S. Image segmentation using active contours with normally biased GVF external force. *IEEE Signal Process Lett.* (2010) 17:875–8. doi: 10.1109/LSP.2010.2060482
41. Wang Y, Jia Y. External Force for Active Contours: Gradient Vector Convolution, In: *PRICAI: Trends in Artificial Intelligence, LNAI.* (2008) 5351:466–472.
42. Park H, Chung M. External force of snake: virtual electric field. *IEE Electron Lett.* (2002) 38:1500–2. doi: 10.1049/el:20021037
43. Sum KW, Cheung YS. Boundary vector field for parametric active contours. *Pattern Recognit.* (2007) 40:1635–45. doi: 10.1016/j.patcog.2006.11.006
44. Jifeng N, Chengke W, Shigang L, Shuqin Y. NGVF: an improved external force field for active contour mode. *Pattern Recognit Lett.* (2007) 28:58–63. doi: 10.1016/j.patrec.2006.06.014
45. Cheng J, Foo SW. Dynamic directional gradient vector flow for snakes. *IEEE Trans Image Process.* (2006) 15:1563–71. doi: 10.1109/TIP.2006.871140
46. Li C, Liu J, Fox MD. Segmentation of external force field for automatic initialization and splitting of snakes. *Pattern Recognit.* (2005) 38:1947–60. doi: 10.1016/j.patcog.2004.12.015
47. Lu S, Wang Y. Gradient vector flow over manifold for active contours. In: *Proceedings of the 9th Asian Conference on Computer Vision. ACCV.* (2009). p. 147–56.
48. Le Y, Xu X, Zha L, Zhao W, Zhu Y. Fast gradient vector flow computation based on augmented Lagrangian method. *Pattern Recognit Lett.* (2013) 34:219–25. doi: 10.1016/j.patrec.2012.09.017
49. Jaouen V, González P, Stute S. Variational segmentation of vector-valued images with gradient vector flow. *IEEE Trans Image Process.* (2014) 23:4773–85. doi: 10.1109/TIP.2014.2353854
50. Battiato S, Farinella GM, Puglisi G. Saliency-based selection of gradient vector flow paths for content aware image resizing. *IEEE Trans Image Process.* (2014) 23:2081–95. doi: 10.1109/TIP.2014.2312649
51. Miri MS, Robles VA, Abramoff MD. Incorporation of gradient vector flow field in a multimodal graph-theoretic approach for segmenting the internal limiting membrane from glaucomatous optic nerve head-centered SD-OCT volumes. *Comp Med Imag Graph.* (2017) 55:87–94. doi: 10.1016/j.compmedimag.2016.06.007
52. Abdullah M, Dlay S, Woo W, Chambers J. Robust iris segmentation method based on a new active contour force with a noncircular normalization. *IEEE Trans Syst Man Cybernet.* (2017) 47:3128–41. doi: 10.1109/TSMC.2016.2562500
53. Kirimasthong K, Rodtook A, Chaumrattanakul U, Makhanov SS. Phase portrait analysis for automatic initialization of multiple snakes for segmentation of the ultrasound images of breast cancer. *Pattern Anal Appl.* (2017) 20:239–51. doi: 10.1007/s10044-016-0556-9
54. Keatmanee C, Chaumrattanakul U, Kotani K, Makhanov SS. Initialization of active contours for segmentation of breast cancer via fusion of ultrasound, doppler, and elasticity images. *Ultrasonics.* (2019) 94:438–453. doi: 10.1016/j.ultras.2017.12.008
55. Kirimasthong K, Rodtook A, Lohitvisate W, Makhanov SS. Automatic initialization of active contours in ultrasound images of breast cancer. *Pattern Anal Appl.* (2018) 21:491–500. doi: 10.1007/s10044-017-0627-6
56. Rodtook A, Kirimasthong K, Lohitvisate W, Makhanov SS. Automatic initialization of active contours and level set method in ultrasound images of breast abnormalities. *Pattern Recognit.* (2018) 79:172–182. doi: 10.1016/j.patcog.2018.01.032
57. Jaouen V, Bert J, Bousson N, Fayad H, Hatt M, Visvikis D. Image enhancement with PDEs and nonconservative advection flow fields. *IEEE Transact Image Process.* (2019) 28:3075–3088. doi: 10.1109/TIP.2018.2881838
58. Li K, Wang Y. Image structure adaptive gradient vector flow for active contours. *Int Conf Inf Eng Comp Sci.* (2009) 3:1572–4. doi: 10.1109/ICIECS.2009.5366000
59. Weickert J. Coherence-enhancing diffusion filtering. *Int J Comput Vis.* (1999) 31:111–27. doi: 10.1023/A:1008009714131